Phosphorylation-inducing chimera rewires oncogenic kinase to trigger apoptosis

Manuel L. Merz[1,¶], Veronika M. Shoba[1,¶], Rajaiah Pergu[1,2,3,¶], Zachary C. Severance[1,¶], Dhanushka N. P. Munkanatta Godage[1], Arghya Deb[1], Hui Si Kwok[4,5], Prashant Singh[1], Sameek Singh[1], Jonathan B. Allen[9], Wenzhi Tian[1], Pallavi M. Gosavi[4,5], Santosh K. Chaudhary[1], Viktoriya Anokhina[1], Ellen L. Weisberg[6], N. Connor Payne[4,7,8], Yao He[5,6], Reilly Osadchey[9], Mrinal Shekhar[10], Ralph Mazitschek[5,7,8], Matthew G. Rees[5], Jennifer A. Roth[5], Qiang Cui[9,11,12], James D. Griffin[6], Brian B. Liau[4,5], and Amit Choudhary[1,2,3,*]

[1]Chemical Biology and Therapeutics Science Program, Broad Institute of MIT and Harvard, Cambridge, MA 02142, USA
[2]Divisions of Renal Medicine and Engineering, Brigham and Women's Hospital, Boston, MA 02115, USA
[3]Department of Medicine, Harvard Medical School, Boston, MA 02115, USA
[4]Department of Chemistry and Chemical Biology, Harvard University, Cambridge, MA, USA
[5]Broad Institute of MIT and Harvard, Cambridge, MA, 02142, USA
[6]Department of Medical Oncology, Dana-Farber Cancer Institute, Boston, MA 02215, USA
[7]Center for Systems Biology, Massachusetts General Hospital, Boston, MA, 02114, USA
[8]Harvard T.H. Chan School of Public Health, Boston, MA, 02115, USA
[9]Department of Chemistry, Boston University, Boston, MA 02215, USA
[10]Center for the Development of Therapeutics, Broad Institute of MIT and Harvard, Cambridge, MA 02142, USA
[11]Department of Physics, Boston University, Boston, MA 02215, USA
[12]Department of Biomedical Engineering, Boston University, Boston, MA 02215, USA

¶These authors contributed equally to this work and are listed arbitrarily. They will put their name first in their curriculum vitae citations or elsewhere.

*To whom correspondence should be addressed:

Amit Choudhary
Chemical Biology and Therapeutics Science Program
Broad Institute of MIT and Harvard
415 Main Street, Rm 3012
Cambridge, MA 02142
Phone: (617)714-7445
Fax: (617)715-8969
Email: achoudhary@bwh.harvard.edu

ABSTRACT

Hyperactive enzymes drive the pathology of several diseases, and classically, “occupancy-driven” drugs (e.g., active site or allosteric inhibitors) are used to target these enzymes. However, the stoichiometric nature of such inhibitors and the emergence of resistance highlight the need for new modalities. Here, we report a Phosphorylation-Inducing Chimeric Small molecule (PHICS) that rewires the hyperactivity of an oncogenic kinase, BCR-ABL, to phosphorylate its active site residue. Molecular dynamics simulations suggest this phosphorylation inhibits BCR-ABL by inducing electrostatic rearrangements of its active site. This “event-driven” mechanism selectively induces apoptosis of BCR-ABL-dependent cancer cells at substoichiometric concentrations (vs. stoichiometric concentrations of occupancy-driven drugs). Furthermore, PHICS is effective on other oncogenic ABL fusions or clinically observed resistance mutations, including to occupancy-driven drugs with the same binding site as PHICS, pointing to the orthogonality of their resistance mechanisms. These studies lay the foundation for electric-field and “event-driven” modalities to control hyperactive enzymes with orthogonal resistance mechanisms to occupancy-driven modalities.

KEYWORDS: BCR-ABL, PHICS, phosphorylation, induced proximity, event-driven pharmacology, resistance development, CRISPR-suppressor scanning

INTRODUCTION

Aberrant enzymatic activity is the etiological factor in many disorders. For example, the hyperactivity of oncogenic kinase BCR-ABL results in uncontrolled cell growth, triggering chronic myelogenous leukemia (CML) and other myeloproliferative disorders.[1-4] Inhibitory phosphorylations are natural regulatory modifications[5-7] and we can potentially induce such modifications using phosphorylation-inducing chimeric small molecules (PHICS)[8-10] that foster proximity between a kinase and target protein to induce the latter's phosphorylation. Since certain BCR-ABL phosphorylations are inhibitory,[11] we hypothesized that PHICS could potentially rewire BCR-ABL's elevated activity to induce such phosphorylation onto itself, thereby providing an autoinhibition mechanism with several attractive attributes. First, these PHICS will operate by an "event-driven mechanism"[12-15] vs. the "occupancy-driven mechanism" of active site or allosteric inhibitors that require sustained BCR-ABL occupancy for the pharmacological effect. PHICS-induced inhibitory phosphorylation will persist even after dissociation from BCR-ABL, enabling turnover and sub-stoichiometric potency.[16] Second, PHICS will have different resistance mechanisms from occupancy-driven inhibitors, for which resistance has rapidly emerged.[17-20] Third, the requirement of both binding and phosphorylation induction events provides an additional layer of selectivity that may reduce off-targets.[21] Finally, since PHICS can be developed from kinase inhibitors,[10] this approach is potentially generalizable to other oncogenic kinases and enzymes.

Here, we report PHICS **11** (generated by homo-dimerizing ABL binders) that formed a ternary complex with BCR-ABL and induced inhibitory phosphorylation at Y253 that rewires the electrostatic arrangement of residues in the active site. PHICS **11** potently induces apoptosis of BCR-ABL-dependent cancer cells at low nanomolar concentration, which is ~20-fold lower than required for complete BCR-ABL occupancy by PHICS **11**, suggesting turnover. PHICS **11** was also active in cells harboring gatekeeper mutation (T315I) that renders active-site drugs (e.g., imatinib) ineffective and in cells with other oncogenic ABL fusions (e.g., TEL-ABL) that are resistant to approved drugs (e.g., asciminib).[3, 22, 23] CRISPR-based mutagenesis studies showed that PHICS **11**, which binds to the same site as the allosteric inhibitor asciminib, was effective in asciminib-resistant cells and exhibited a resistance profile distinct from that of asciminib. PHICS **11** showed selectivity for BCR-ABL dependent cancer cells in a pooled screening of ~1000 cancer cells of diverse lineages and genotypes. Overall, PHICS **11**

introduces a fundamentally new modality that operates by electric-field effects and event-driven mechanism to target an oncogenic enzyme with resistance mode orthogonal to occupancy-based drugs.

RESULTS

PHICS 11 potently inhibits the growth of BCR-ABL-dependent K562 cells. We have previously reported that PHICS can rewire kinase specificity to induce inhibitory phosphorylations on oncogenic targets and death of

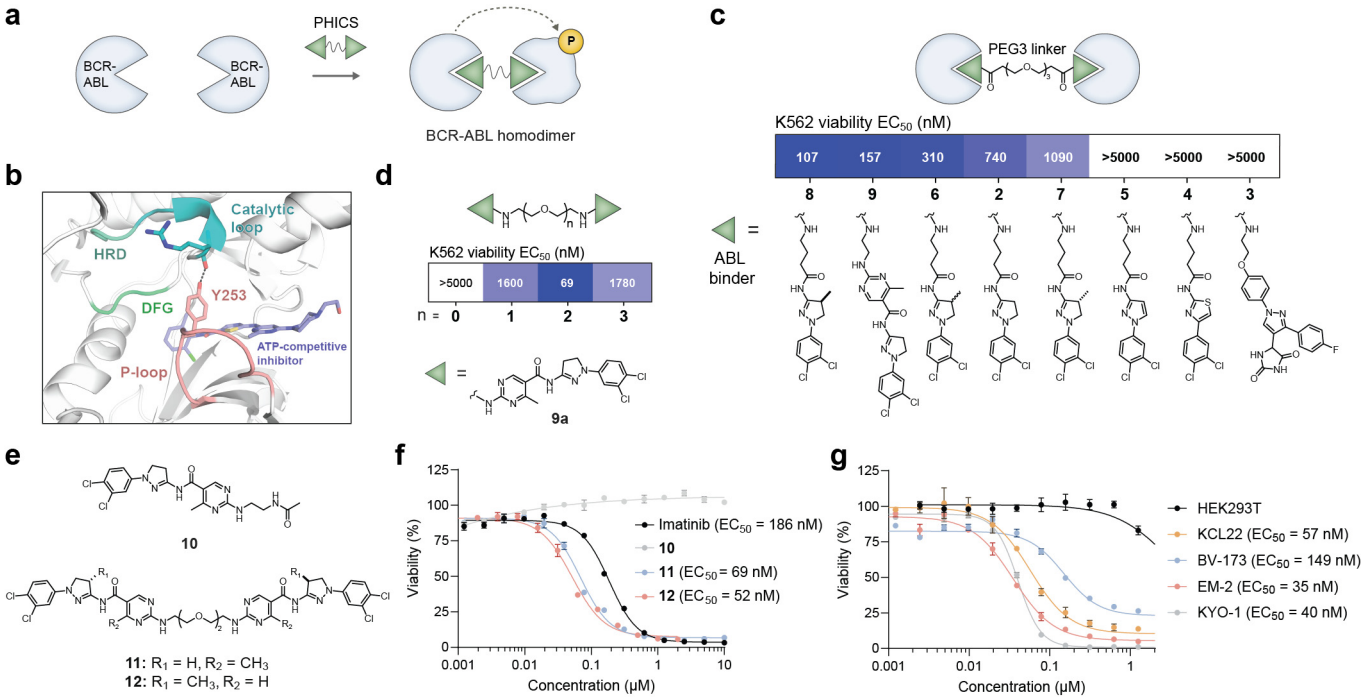

Figure 1. Development of potent inhibitor of BCR-ABL oncogenesis. a Dimerization of BCR-ABL with PHICS catalyzes inhibitory autophosphorylation. **b** Co-crystal structure of ABL and ATP competitive inhibitor dasatinib (PDB 2GQG). DFG motif, catalytic loop with HRD motif, and hydrogen bonding of Y253 (black dotted line) are shown. P-loop residues 248–255 are highlighted. **c** Structure-activity relationship of BCR-ABL PHICS. PEG3 linker was used to join different ABL activators, and cytotoxicity in K562 cells expressing BCR-ABL was measured. **d** Different PEG linkers were used to join two ABL ligands **9a,** and cytotoxicity in K562 cells was measured. **e** Structures of optimized PHICS (**11** and **12**) and respective ABL activator control (**10**). **f** Dose response for cytotoxicity in K562 for different BCR-ABL inhibitors (**11**, **12**, imatinib) and the control ABL binder **10**. **g** Cytotoxicity of PHICS **11** in HEK293T and different cell lines expressing the oncogenic BCR-ABL fusion. EC_{50} values in **c** and **d** were calculated from three independent replicates. **f** and **g** show the mean and SD of three independent replicates.

cancer cells.[10] Motivated by this observation, we hypothesized that a homodimer of ABL binders might also inhibit BCR-ABL by inducing inhibitory phosphorylation (**Fig. 1a**).[24, 25] Towards that goal, we synthesized homodimer **2** by connecting ABL binder **1** from a solvent-exposed site[26] (**Supplementary Fig. 1a-c**) and used mass spectrometry to assess alteration in phosphorylation levels of ABL in the presence of **2**. We were gratified to see an increase in levels of Y253 phosphorylation of ABL in the presence of **2**, while such phosphorylation was undetectable in DMSO or monomer **1** treated ABL (**Supplementary Fig. 1d**). Previous studies[11] have shown

that phosphorylation at Y253, which is part of the ATP-binding loop (P-loop) and proximal to the DFG motif, reduces BCR-ABL oncogenicity (**Fig. 1b**). In agreement with these studies, **2** reduced the viability of BCR-ABL dependent K562 cells with an EC_{50} of 740 nM (**Supplementary Fig. 1e**).

Using the viability of K562 cells as a readout, we performed structure-activity relationship studies by systematically varying the linker between the previously reported ABL binders (**Fig. 1c and Supplementary Fig. 2a**). Compounds **3** (hydantoin scaffold),[27] **4** (thiazole scaffold) and **5** (pyrazole scaffold) exhibited loss of activity (EC_{50} > 5000 nM). Compound **6**, which is assembled from a methylated analog derived from the dihydropyrazole scaffold of **2,** exhibited increased K562 cytotoxicity (EC_{50} = 310 nM) in agreement with prior studies[26] that methylation of the dihydropyrazole scaffold increases ABL activation by 1.3 fold. Furthermore, the *S*-enantiomer (**8**) of compound **6** is approximately 10-fold more potent than the (*R*) enantiomer (**7**) (EC_{50} = 107 nM and 1090 nM, respectively), in agreement with their reported degree of ABL activation. Finally, linking a methyl pyrimidine on the amino dihydropyrazole through an amide bond afforded compound **9**, which displayed comparable activity to **8** (EC_{50} = 157 nM). Using a methyl pyrimidine scaffold **9a** for synthetic simplicity and avoiding the chiral centers in **8**, we varied the length of PEG linkers (n = 0–3) between the two ABL binders and identified PEG2 (**11**) as optimal, achieving an EC_{50} of 69 nM (**Fig. 1d,e and Supplementary Fig. 2b**). Substituting the methyl group from pyrimidine to (*S*)-4-methyl dihydropyrazole further improved potency slightly (**12**, EC_{50} = 52 nM). However, due to minimal gain and challenges with chiral purification, we proceeded with **11** as the optimized molecule. Notably, **11** exhibited higher potency than the first-in-class BCR-ABL drug imatinib in reducing the viability of K562 cells (**Fig. 1f**). Next, we confirmed the activity of **11** in other BCR-ABL positive CML cell lines (KCL22, BV-173, EM-2 and KYO-1). We observed dose-dependent cytotoxicity (EC_{50}: 35–149 nM), but not on HEK293T cells that lack BCR-ABL (EC_{50}: > 3000 nM, **Fig. 1g**). The observed dependence of compound activity on linker length, the potency of ABL activation by the binder scaffold, and BCR-ABL dependence points to an induced-proximity mechanism, which we investigated next.

PHICS 11 promotes ternary-complex formation and induces Y253 phosphorylation on BCR-ABL. We first assessed the binding of PHICS to ABL using differential scanning fluorimetry (DSF). Compounds **11** and **10** increased the protein melting temperature (T_m), indicative of ABL-binding (**Supplementary Fig. 3a–c**). We

established a TR-FRET assay to monitor binding to the myristoyl allosteric pocket (**Supplementary Fig. 3d-e**). Here, the TR-FRET signal is observed when the tracer (derived from an allosteric myristoyl pocket binder) is in proximity to a CoraFluor-labeled anti-GST nanobody donor—thus, signal decrease upon competitive displacement of the tracer by **11** measures target engagement.[28] As expected, PHICS **11,** ABL binder **10** (**Fig. 2a**), and asciminib (**Supplementary Fig. 3f**) reduced the TR-FRET signal dose-dependently, consistent with their overlapping binding pocket. Next, we used analytical ultracentrifugation to confirm ternary complex formation by **11**. Compound **11**, but not vehicle or **10**, caused a shift in the sedimentation coefficient, consistent with ABL dimerization (**Fig. 2b**).

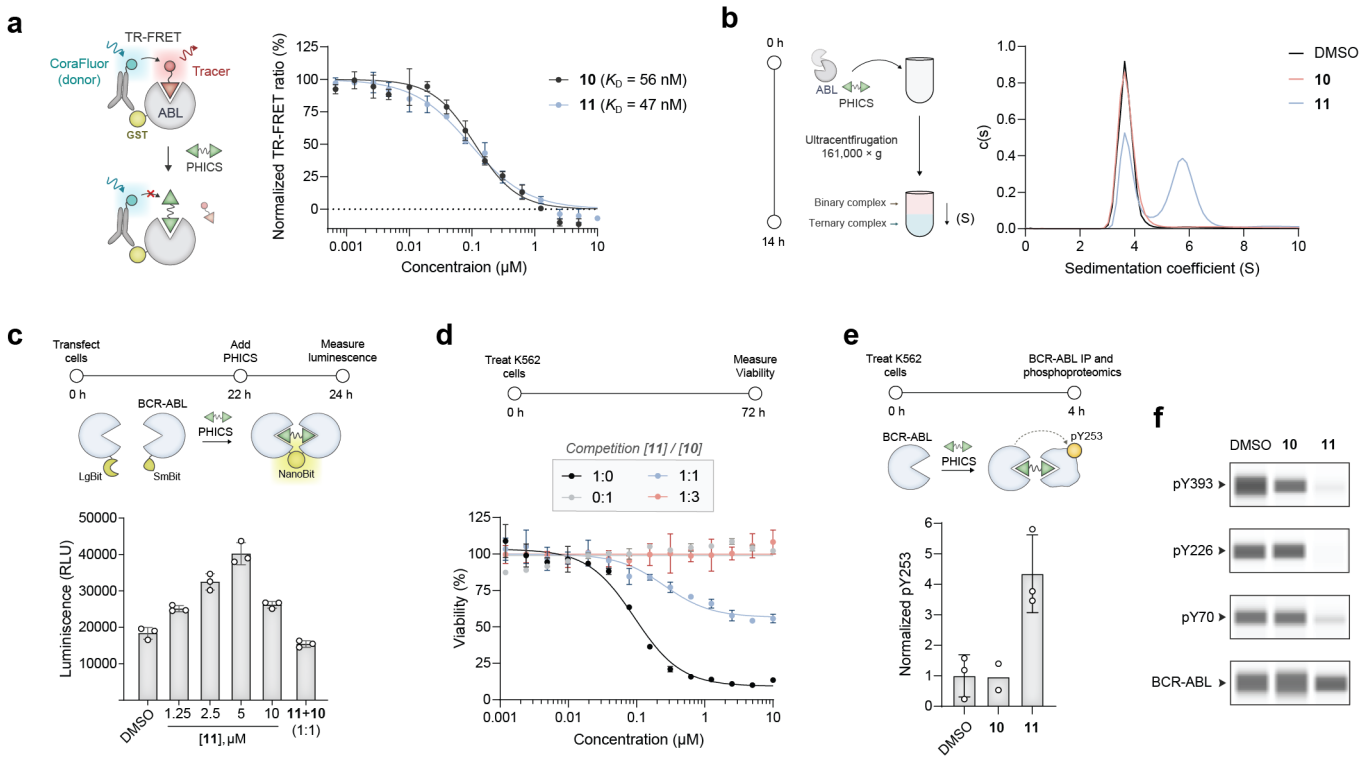

Figure 2. Assessment of ternary complex formation and phosphorylation induction by PHICS 11. a TR-FRET assay to confirm binding to the allosteric myristoyl pocket of the ABL kinase. Dose-dependent displacement of the tracer by PHICS **11** and control **10** was measured. Mean and SD of three independent replicates are shown. **b** Analytical ultracentrifugation to measure the sedimentation coefficient and biochemical ternary complex formation of the ABL kinase in the presence of either **11** or its control **10** (1.5 μM). **c** Dose-dependent cellular ternary complex formation by **11** in HEK293T cells transfected with LgBiT and SmBiT BCR-ABL. For competition, a 1:1 ratio of **10** to **11** was added (5 μM each). Mean and SD for three independent replicates are shown. **d** Rescue of dose-dependent cytotoxicity of **11** in K562 cells. Mean and SD of three independent replicates are shown. **e** Phosphorylation analysis by LC-MS/MS. Relative phosphorylation levels to unmodified peptides were measured after treatment with either **11** or its control **10**. Vehicle (DMSO) and **11**-treated samples were measured in three independent replicates, while **10** was measured in duplicates. Mean and SD (for **11** and DMSO) are shown. **f** Immunoblotting to probe autophosphorylation on BCR-ABL after treatment of K562 cells with of either **11** (1 μM) or **10** (2 μM). A representative example for three independent measurements is shown.

To further confirm ternary complex formation in cells, we used a split luciferase NanoBiT assay, where BCR-ABL constructs were fused to luciferase components LgBit and SmBit (**Fig. 2c**). Treatment with **11** increased luminescence, indicating ternary complex formation, while competition with **10** reduced the signal. Indicative of an induced-proximity mechanism, we observed a characteristic "hook effect"[29] by increasing the concentration of **11**. In agreement with these findings, we found that ABL binder **10**, which is not cytotoxic to K562 cells, rescued the killing activity of **11** when K562 cells were co-treated with **10** and **11** (**Fig. 2d**). To determine alteration in BCR-ABL phosphorylation, we performed mass spectrometry on immunoprecipitated BCR-ABL from K562 cells treated with DMSO, **10**, or **11** (**Fig. 2e**). While treatment with **10** had similar phosphorylation levels at Y253 to the vehicle (DMSO), **11** selectively increased phosphorylation at Y253. Phosphorylation at Y253 correlates with reduced BCR-ABL activity[11] and in agreement with these studies, we observed reduced autophosphorylation at multiple activation sites on BCR-ABL (pY70, pY226, and pY393) in **11**-treated K562 cells using immunoblotting (**Fig. 2f**).[1, 3, 30] We further performed a global phosphoproteomic analysis and confirmed increased Y253 phosphorylation and decreased phosphorylation at sites correlating with autoactivation (pY226 and pY393). In contrast, the global proteome was comparably unaltered relative to DMSO treatment (**Supplementary Fig. 3g–i**). These findings suggest that **11** forms a ternary complex with a BCR-ABL homodimer to selectively promote Y253 phosphorylation.

Classical molecular dynamics (MD) simulations offer a plausible mechanism for inhibiting BCR-ABL caused by Y253 phosphorylation. In the apo state, phosphorylation of Y253 (Y253TP2) is observed to induce a significant conformational change in the P-loop, leading to the formation of a salt bridge between the phosphate group with R367 that obstructs ATP binding (**Fig. 3a and Supplementary Fig. 4a,b**). Electrostatic potential calculations further reveal that Y253 phosphorylation enhances the negative potential of the active site, disfavoring the binding of ATP's triphosphate moiety (**Fig. 3b,c**). Simulations of activated BCR-ABL in complex with ATP · Mg^{2+} also suggest that phosphorylation of Y253 impedes the catalytic competency. Intuitively, one might expect that the negatively charged Y253TP2 and ATP would strongly repel each other. Instead, the MD simulations suggest that the high negative charge density draws sodium ions into the binding pocket, forming a stable ionic cluster (compare **Fig. 3d,e**) between Y253TP2's phosphate group, ATP's triphosphate moiety, R367, and three to four sodium cations (**Fig. 3e,f and Supplementary Fig. 4c,d**). The formation of this tightly packed

cluster causes inversion of the P-loop and prevents access to ATP's γ-phosphate, thereby precluding substrate phosphorylation.

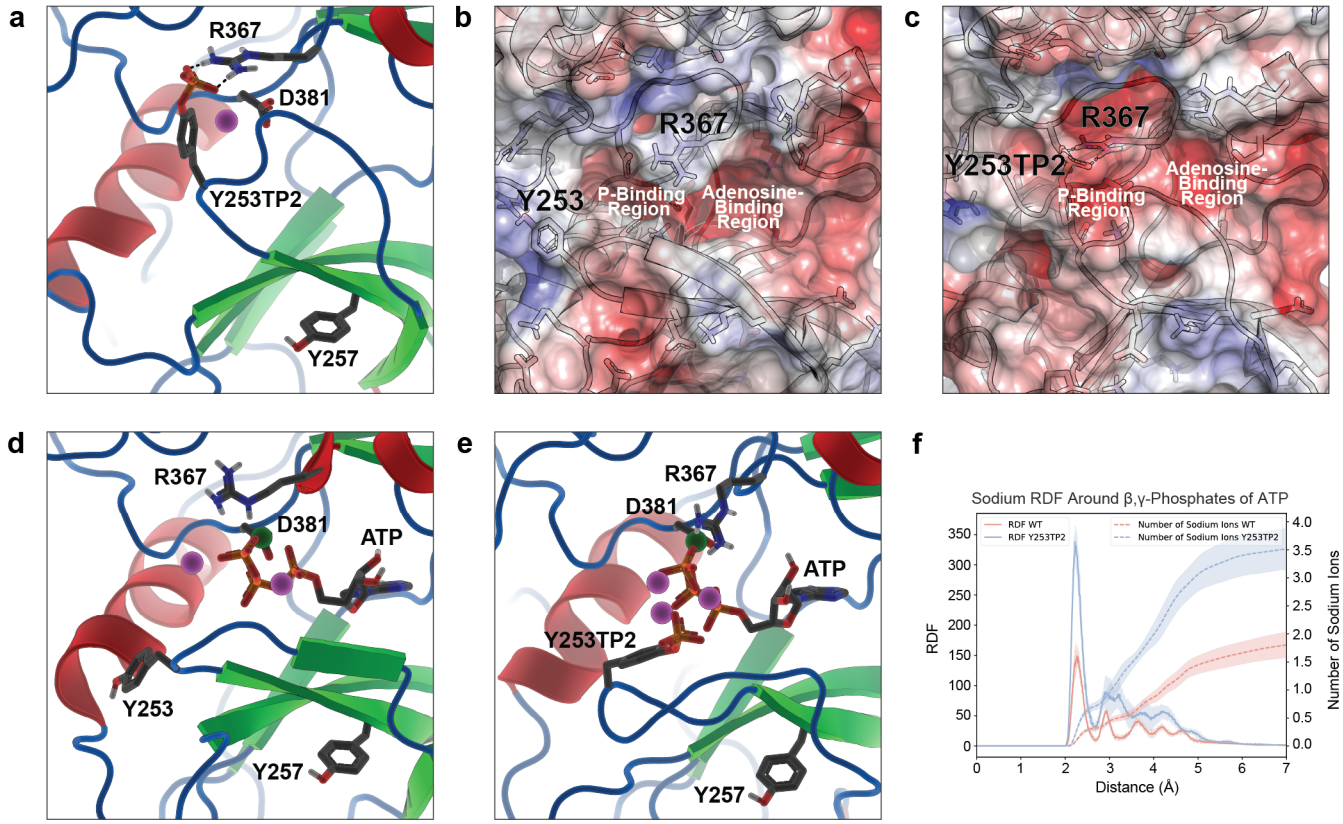

Figure 3. MD simulations suggest an inhibitory mechanism of Y253 phosphorylation. a Phosphorylation of Y253 (Y253TP2) in the apo state results in salt bridge formation with R367, blocking ATP binding. A nearby Na^+ ion (violet sphere) neutralizes the ion pair's net charge. **b–c** Electrostatic potential of BCR-ABL binding pocket in the (**b**) wild-type and (**c**) Y253TP2 apo states. Scale ranges from -5 (red) to +5 (blue) $k_B T/e$, where k_B is Boltzmann's constant, e is the elementary charge, and T = 303.15 K. **d–e** Snapshots of BCR-ABL complexed to ATP · Mg^{2+} in (**d**) wild-type and (**e**) Y253TP2 states illustrate the formation of an ionic cluster formed by the phosphorylated Y253, the *β,γ*-phosphates of ATP, R367 and several Na^+ ions that impedes the kinase function. Na^+ and Mg^{2+} ions are shown as violet and dark green spheres, respectively. **f** Radial distribution functions of Na^+ ions around the *β,γ*-phosphates of ATP in the wild-type (red) vs. Y253TP2 (blue) states demonstrate increased concentration of Na^+ ions within the active site following Y253 phosphorylation. The dashed lines indicate the integrated number of Na^+ ions up to a distance to the center of *β,γ*-phosphates of ATP. The shaded area indicates statistical uncertainty.

PHICS 11 inhibits BCR-ABL signaling. We next sought to investigate the effects of **11** on BCR-ABL signaling. Treatment of K562 cells with **11** (1 μM) inhibited substrate phosphorylation and downstream signaling pathways of BCR-ABL, including pSTAT5, pERK, and pCRKL,[1, 3, 31] while the ABL binder **10** (2μM) had no effect (**Fig. 4a**). We observed cleavage of both caspase 8 and PARP, consistent with induction of apoptosis by **11** upon inhibition of BCR-ABL signaling (**Fig. 4b**). Collectively, these findings demonstrate that PHICS **11** reduce the viability of BCR-ABL-dependent cell lines by selectively inducing apoptosis and suppressing the oncogenic BCR-ABL signaling. Finally, we compared the transcriptomic effects of **11**, the allosteric inhibitor asciminib, and

the ABL binder **10** using RNA sequencing (RNA-seq). K562 cells were treated with DMSO (vehicle), asciminib (100 nM), **11** (1 μM), or **10** (2 μM) for 6, 12, or 24 hours in biological quadruplicates. Gene expression levels were analyzed using replicate PCA plots, gene set enrichment analysis (GSEA), and moderated t-tests to compare treatment groups (**Fig. 4c,d, and Supplementary Fig. 5a–f**). We observed nearly identical gene expression profiles for cells treated with **11** and asciminib (Group A in **Fig. 4d**). Similarly, the gene expression profiles for the vehicle control and **10** were almost indistinguishable, confirming that the ABL binder **10** is not cytotoxic and behaves similarly to the vehicle. Remarkably, these findings suggest that converting the allosteric binder for ABL into a PHICS transforms a ligand with no detectable effects, comparable to the vehicle control, into a potent and selectively cytotoxic compound that induces gene expression changes closely matching those of a clinically approved drug.

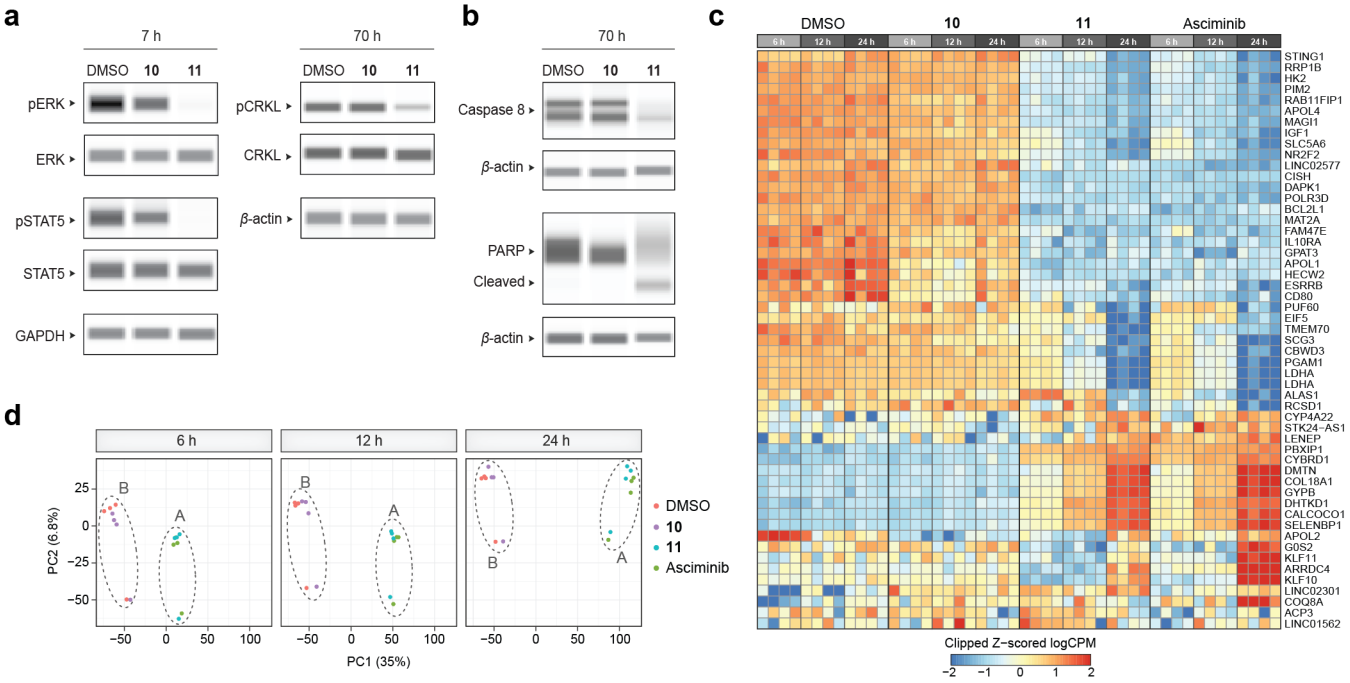

Figure 4. PHICS 11 disrupts BCR-ABL signaling pathway. a Inhibition of BCR-ABL downstream signaling. K562 cells were treated with either PHICS **11** (1 μM) or its control **10** (2 μM), and pSTAT5, pERK, and pCKRL were measured relative to the respective total protein level. **b** Activation of pro-apoptotic pathways. Immunoblotting after 70-hour incubation with either PHICS **11** (1 μM) or its control **10** (2 μM) is shown. Immunoblotting experiments in **a** and **b** were measured in at least three independent replicates, and a single representative example is shown. **c** Global transcriptomic analysis in K562 cells treated with DMSO, **10**, **11**, or asciminib. Equal number of genes scoring the highest p-values for each comparison are shown. **d** PCA plot for gene expression analysis. Cluster A is formed by **11** and asciminib, while cluster B is formed by DMSO and **10**. Gene expression was analyzed across four independent biological replicates.

PHICS 11 selectively inhibits BCR-ABL and other oncogenic ABL fusions. Beyond BCR-ABL, several other oncogenic ABL fusions are known.[3] These different fusion partners can change the localization, catalytic efficiency, sensitivity to inhibitors, and substrate preferences of the kinase.[32, 33] For example, the TEL-ABL fusion has much higher *in vitro* and *in vivo* activity than BCR-ABL. To thus test **11** against these alternative fusion proteins, we treated Ba/F3 cells expressing TEL-ABL with **11**, which reduced the viability with an EC_{50} value of 280 nM (**Fig. 5a**). In contrast, the clinically approved allosteric ABL-inhibitor, asciminib,[34, 35] which binds to the same myristoyl pocket as **11**, did not affect the cell viability. However, the low efficacy of asciminib is not a result of reduced binding affinity, as the addition of one equivalent of asciminib reversed the effect of **11** (**Fig. 5a**). This not only demonstrates that **11** potently inhibits the viability of different oncogenic ABL-fusions, but also highlights that they exhibit a unique mode of action that differs from classical occupancy-driven inhibitors such as asciminib.

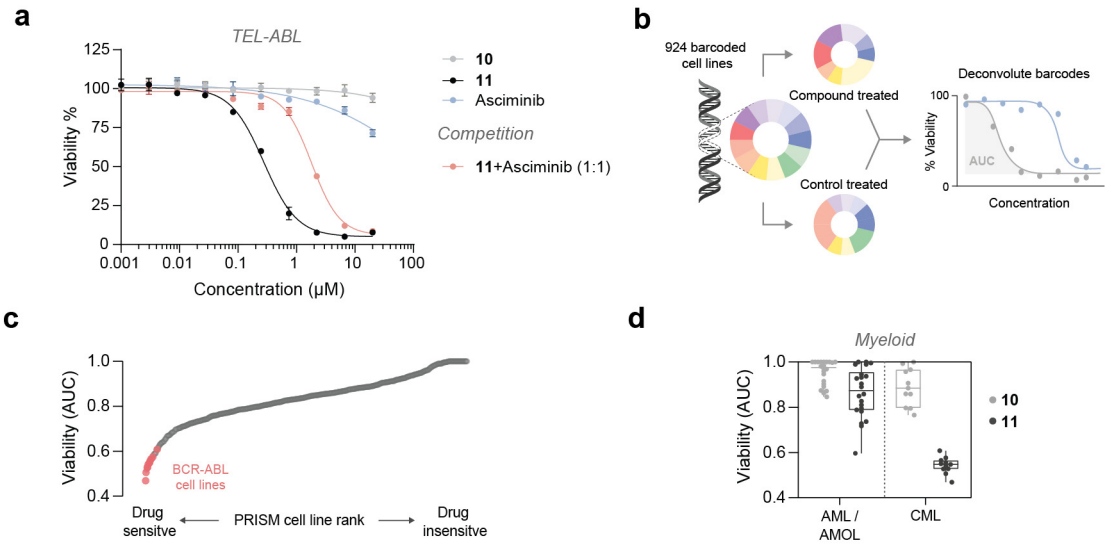

Figure 5. PHICS 11 is effective against oncogenic ABL fusions. a Cytotoxicity in Ba/F3 cells expressing TEL-ABL. Mean and SD of three independent replicates are shown. **b** Schematic of the PRISM screening. Barcoded cell lines were incubated for 5 days with either **11**, **10**, or imatinib in an 8-point and 3-fold serial dilution. **c** Ranking of PRISM cell lines according to sensitivity for **11**. Cell lines annotated BCR-ABL positive by the DepMap portal are highlighted. **d** Boxplot showing lineage-specific sensitivity to **11** and **10**. The box extends from the first to third quartiles, the median is depicted as center line, and the whiskers depict the range. PRISM screen was performed in three independent replicates (n = 3).

To evaluate the selectivity of **11** and gain a comprehensive understanding of its activity in CML and other contexts, we conducted PRISM multiplexed screening on 924 barcoded cancer cell lines originating from various tissues with diverse genetic backgrounds (**Fig. 5b**).[36] Crucially, the DepMap portal annotates cell lineages and oncogenic features, enabling targeted analysis of differential responses between cell types, such as those expressing oncogenic ABL fusions.[37] We treated cell pools with either **11** or the ABL binder **10** in a 5-day viability

assay, using an 8-point dose range (3-fold dilution). Among the tested cell lines, eleven were annotated as BCR-ABL positive and exhibited increased sensitivity to **11**, ranking among the top 33 most drug-responsive cell lines (top 3.6% of the 924 tested; **Fig. 5c**). In contrast, the ABL binder **10** showed no considerable inhibitory effect on the BCR-ABL positive cell lines (**Supplementary Fig. 6a**). A side-by-side analysis of **11** and imatinib revealed comparable sensitivity profiles, converging on the targeting of cell lines expressing BCR-ABL fusions (**Supplementary Fig. 6b**). Notably, the previously studied cell lines, including K562, KCL22, BV-173, EM-2, and KYO-1, also displayed increased sensitivity to both **11** and imatinib in the PRISM screen ($AUC_{viability} < 0.6$). Further analysis by lineage revealed that myeloid cell lines, specifically those derived from chronic myeloid leukemia (CML), were more sensitive to **11**, while acute myeloid leukemia (AML) cell lines and other lineages showed no clear dependencies (**Fig. 5d and Supplementary Fig. 6c**). These findings indicate that **11** exhibits high selectivity for CML cells dependent on ABL oncogenic fusions, with minimal off-target effects on other cell lines.

PHICS 11 displays an orthogonal resistance mechanism to that of asciminib. Resistance development is a common failure mode of many BCR-ABL targeting inhibitors[1, 38]. Gratifyingly, **11** remained effective against clinically relevant imatinib-resistant E255V and gatekeeper mutant T315I in Ba/F3 cells (**Supplementary Fig. 7a,b**). Since asciminib and **11** bind to the same allosteric pocket but with different inhibition mechanisms, we hypothesized that their resistance mechanisms would differ. To identify resistance mutation hotspots, we performed CRISPR-suppressor scanning.[39, 40] Here, we used the mutagen SpCas9 and a library of guide RNAs (sgRNA) tiling across the coding region of ABL1 to generate a pool of BCR-ABL variants in K562 cells (**Fig. 6a**). We applied dose escalation of **11** or asciminib as a selection pressure over 63 days, increasing the dose at days 14 and 21, which ultimately enriched for cells carrying resistance mutations (**Supplementary Fig. 8a**). We treated enriched cells with either asciminib or **11** (**Fig. 6b and Supplementary Fig. 8b**) and observed a 1000-fold and 3-fold loss in sensitivity for asciminib and **11**, respectively. Interestingly, we identified an orthogonal resistance for **11** and asciminib (**Fig. 6c**), where cells subjected to asciminib remained sensitive to **11** and vice versa.

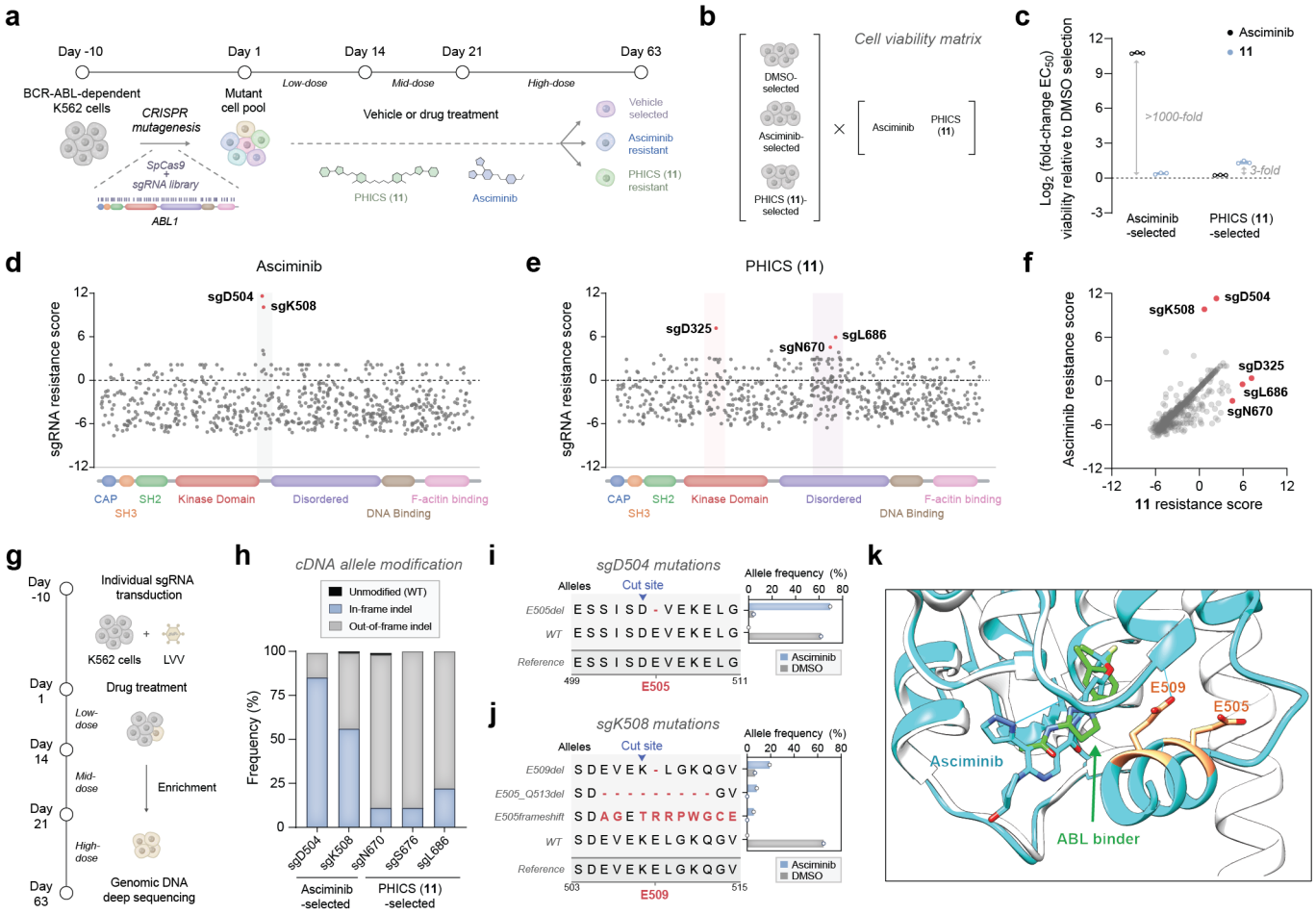

Figure 6. CRISPR-suppressor scanning identifies orthogonal resistance mutations for asciminib and PHICS 11. **a** Schematic workflow for the CRISPR-suppressor scanning. **b–c** Cell viability matrix assay to measure drug-sensitivity after 63 days of selection. Resistance is expressed as $\log_2$-fold change relative to the DMSO selection (**c**). Mean and SD of three independent replicates are shown. **d–e** sgRNA resistance scores in the CRISPR suppressor scanning. K562 cells were collected after 63 days of treatment with either vehicle, asciminib (**d**) or **11** (**e**) following a dose-escalation schedule. Genomic DNA was extracted and sgRNA abundance was determined by sequencing. Scatter plots show resistance scores, calculated as z-scored log2-fold changes in sgRNA abundance in drug-treated conditions relative to the vehicle (DMSO)-treated population. sgRNA selected for further validation are annotated with their predicted cleavage site and highlighted in red. Datapoints represent the mean resistance scores across three replicate treatments. **f** Scatter plot comparing sgRNA resistance scores following 63 days of dose-escalated selection with asciminib or **11**. **g** Schematic for sgRNA validation and analysis of drug-resistant cells. **h** Targeted sequencing of sgRNA target sites and quantification of indel-modified sequences. **i–j** Translation of cDNA allele frequency showing the number of modifications induced by sgD504 (**i**) and sgK508 (**j**). Red residues highlight hotspot mutations E505 and E509. **k** Overlay of co-crystal structures for the myristoyl pocket binding asciminib (cyan, PDB: 5MO4) or the ABL binder in **11** (gray/green, PDB: 6NPU). Mutated residues identified in the CRISPR-suppressor scanning are highlighted in orange on the asciminib-bound structure (cyan).

To further study the divergence in drug resistance, we quantified sgRNA abundance in the pooled screen after 14, 21, and 63 days of selection (**Fig. 6d–e and Supplementary Fig. 8c–h**). After 63 days, asciminib-resistant cells were enriched in sgRNAs targeting residues D504 and K508 ($\log_2$-fold change >9 compared to vehicle-treated cells) near the drug-binding site at the interface between ABL kinase domain and the disordered region (**Fig. 6d**). In contrast, and consistent with the observed weaker resistance, treatment with **11** showed dispersed sgRNA enrichment primarily deep within the disordered region (N670 and L686) or the kinase domain

(D325) (**Fig. 6e**). Interestingly, further comparing sgRNA enrichment between **11** and asciminib revealed a single sgRNA targeting the S676 residue being enriched in both selections after 21 days (**Supplementary Fig. 8h**), before the sgRNA enrichment diverged by day 63 (**Fig. 6f**).

Next, we individually delivered the top enriched sgRNAs in K562 cells to validate the resistance (**Fig. 6g**). We subjected the transduced cells to **11** or asciminib treatment, gradually increasing the drug pressure over 63 days (**Supplementary Fig. 9a**). One sgRNA transduction, sgD325, did not recover growth after 63 days of treatment with **11** and was excluded from further analysis. sgRNAs targeting D504 and K508 conferred a strong resistance against asciminib, shifting the EC_{50} from 5 nM to 6500 nM and 900 nM, respectively (**Supplementary Fig. 9b–e**). Confirming the observed orthogonality from the pooled screen, the same cells did not show resistance against **11**, maintaining an EC_{50} of 60 nM and 59 nM, respectively. Conversely, sgRNA targeting N670, S676, and L686 emerging from the **11** selection showed ubiquitous resistance against both asciminib and **11** but shifted the EC_{50} by less than 10-fold. We genotyped editing outcomes at the sgRNA target sites to identify the underlying resistance mutations. sgD504 and sgK508 transduced K562 cells treated with asciminib showed predominantly in-frame mutations that result in E505 or E509 deletions near its binding site, where drug resistance frequently emerges (**Fig. 6h–j and Supplementary Fig. 9f,g**). In contrast, resistance to **11** caused by sgRNA targeting residues N670, S676, and L686 were characterized by large deletions resulting from frameshifts (**Fig. 6h and Supplementary Fig. 9h-j**). This could lead to a partial loss of BCR-ABL activity, which explains both the impaired growth rate and weaker drug resistance. The distinct deletion patterns around residues E505 and E509 suggest that the myristoyl binding pocket conformation[41] plays a crucial role in the orthogonal drug resistance (**Fig. 6k**). Residues E505 and E509 are proximal to asciminib, but distal when bound to the ABL binder used in **11.** Deleting these residues likely disrupts helical folding or interactions with asciminib, while **11** can effectively bind BCR-ABL regardless of these deletions.

Discussion

PHICS targeting BCR-ABL introduces a fundamentally new modality in both proximity-mediated pharmacology and modulation of aberrant enzymatic activity by exploiting a natural regulatory mechanism of inhibitory phosphorylation via electric field effects. Here, PHICS **11** harnesses the aberrant kinase activity and redirects it

against itself to achieve a pharmacologically beneficial effect. This self-targeting leads to phosphorylation, and the high charge density of the phosphate group significantly perturbs protein structure, stability, dynamics, and electrostatic interactions.[6] MD simulations show that the proximity of the phosphorylation site to the ATP-binding pocket and the DFG/HRD motifs likely invokes multiple inhibitory mechanisms, including perturbation of local BCR-ABL structure, ATP-binding, and kinase-substrate engagement.[5, 42] Because most enzymes feature active sites with serine, threonine, or tyrosine-containing loops,[43] the phosphorylation-based inhibitory mechanism could extend beyond BCR-ABL to other kinases and more broadly to other enzymes. Although our study employs non-inhibitory ABL binders, we have successfully developed PHICS from existing kinase inhibitors via group-transfer chemistry.[10] Thus, extant kinase inhibitors can be repurposed to induce inhibitory phosphorylation on a given kinase. For non-kinase targets, the PHICS design requires selecting a partnering kinase based on the consensus phosphorylation motif and the kinase abundance in the target cell. Notably, our approach bypasses *de novo* ligand discovery and extensive medicinal chemistry optimization, which can be resource and time-intensive. Here, the catalytic turnover also potentially enables rapid attainment of high potency. Thus, by leveraging extant inhibitors, appropriate PHICS that induce inhibitory phosphorylation can be developed rapidly and cost-effectively.

Resistance inevitably develops as cancer cells adapt while drugs remain unchanged, pointing to the need for therapies with orthogonal resistance profiles[38]—PHICS **11** exemplifies this principle. While binding to the same site as asciminib, its distinct mechanism effectively induces apoptosis in asciminib-resistant ABL fusions. CRISPR-suppressor scanning confirmed that **11** can overcome drug resistance mutations against asciminib, showing less than a two-fold reduction in efficacy compared to the ~1000-fold loss observed for asciminib. PHICS **11** was also effective in gatekeeper mutation, but that is not surprising since those mutations occur in the ATP pocket,[1] which is distant from the myristoyl pocket targeted by PHICS **11**. A frequently observed resistance mechanism to event-driven pharmacological agents is the alteration in expression levels of the effector enzyme (e.g., E3 ligase complex for PROTACs), which, unlike BCR-ABL, are often non-essential for cancer survival and growth.[44] Finally, we showed in a PRISM multiplexed cancer cell line screen that **11** does not target non-CML cell lines, comparable to the approved drug imatinib, pointing to the low off-targets.[34] Beyond its therapeutic promise, PHICS may also be an important tool for elucidating new aspects of target biology by synthetically

inducing native or neophosphorylation. Taken together, PHICS delivers a rapid, orthogonal strategy to overcome resistance and expand both research and clinical options in oncology.

ACKNOWLEDGEMENT

This work was supported by the NIH (R01GM132825, R01 GM137606, R01 DK132900, R21AI178690, and R35-GM141930). M.M was supported by the Swiss National Science Foundation (P500PN_214260). Computational resources from ACCESS (project BIO230101) are acknowledged. Part of the computational work was performed on the Shared Computing Cluster, which is administered by Boston University's Research Computing Services. We thank K. Tran (Broad Institute) for assisting with chemical compound characterization and structural analysis. We thank J. Dreyfuss and H. Pan from the Joslin Diabetes Center Bioinformatics and Biostatistics Core for performing the RNA-seq analysis.

NOTES

The authors declare the following competing financial interest: Broad Institute has filed patents claiming inventions to genome editing methods in this manuscript. B.B.L. is a shareholder and member of the scientific advisory board of Light Horse Therapeutics, and receives research support from Ono Pharmaceuticals. A.C. is the scientific founder and is on the scientific advisory board of Photys Therapeutics.

REFERENCES

1. Braun, T.P., Eide, C.A. & Druker, B.J. Response and resistance to BCR-ABL1-targeted therapies. *Cancer Cell* **37**, 530-542 (2020).
2. Nowell, P.C. Discovery of the Philadelphia chromosome: a personal perspective. *The Journal of clinical investigation* **117**, 2033-2035 (2007).
3. Hantschel, O. Structure, regulation, signaling, and targeting of abl kinases in cancer. *Genes & cancer* **3**, 436-446 (2012).
4. Ren, R. Mechanisms of BCR–ABL in the pathogenesis of chronic myelogenous leukaemia. *Nature Reviews Cancer* **5**, 172-183 (2005).
5. Ardito, F., Giuliani, M., Perrone, D., Troiano, G. & Lo Muzio, L. The crucial role of protein phosphorylation in cell signaling and its use as targeted therapy. *International journal of molecular medicine* **40**, 271-280 (2017).
6. Johnson, L.N. & Lewis, R.J. Structural basis for control by phosphorylation. *Chem Rev* **101**, 2209-2242 (2001).
7. Seok, S.H. Structural Insights into Protein Regulation by Phosphorylation and Substrate Recognition of Protein Kinases/Phosphatases. *Life (Basel)* **11** (2021).
8. Siriwardena, S.U. *et al.* Phosphorylation-Inducing Chimeric Small Molecules. *Journal of the American Chemical Society* **142**, 14052-14057 (2020).
9. Shoba, V.M. *et al.* Synthetic reprogramming of kinases expands cellular activities of proteins. *Angewandte Chemie* **134**, e202202770 (2022).
10. Pergu, R. *et al.* Development and Applications of Chimera Platforms for Tyrosine Phosphorylation. *ACS Central Science* **9**, 1558-1566 (2023).
11. Skaggs, B.J. *et al.* Phosphorylation of the ATP-binding loop directs oncogenicity of drug-resistant BCR-ABL mutants. *Proceedings of the National Academy of Sciences* **103**, 19466-19471 (2006).
12. Békés, M., Langley, D.R. & Crews, C.M. PROTAC targeted protein degraders: the past is prologue. *Nature Reviews Drug Discovery* **21**, 181-200 (2022).
13. Lai, A.C. & Crews, C.M. Induced protein degradation: an emerging drug discovery paradigm. *Nat Rev Drug Discov* **16**, 101-114 (2017).
14. Modell, A.E., Lai, S., Nguyen, T.M. & Choudhary, A. Bifunctional modalities for repurposing protein function. *Cell Chemical Biology* **28**, 1081-1089 (2021).
15. Singh, S. *et al.* Proximity-inducing modalities: the past, present, and future. *Chemical Society Reviews* **52**, 5485-5515 (2023).
16. Bondeson, D.P. *et al.* Catalytic in vivo protein knockdown by small-molecule PROTACs. *Nature Chemical Biology* **11**, 611-617 (2015).
17. Gorre, M.E. *et al.* Clinical resistance to STI-571 cancer therapy caused by BCR-ABL gene mutation or amplification. *Science* **293**, 876-880 (2001).
18. Shah, N.P. *et al.* Multiple BCR-ABL kinase domain mutations confer polyclonal resistance to the tyrosine kinase inhibitor imatinib (STI571) in chronic phase and blast crisis chronic myeloid leukemia. *Cancer Cell* **2**, 117-125 (2002).
19. Branford, S. *et al.* High frequency of point mutations clustered within the adenosine triphosphate-binding region of BCR/ABL in patients with chronic myeloid leukemia or Ph-positive acute lymphoblastic leukemia who develop imatinib (STI571) resistance. *Blood* **99**, 3472-3475 (2002).
20. Hochhaus, A. *et al.* Molecular and chromosomal mechanisms of resistance to imatinib (STI571) therapy. *Leukemia* **16**, 2190-2196 (2002).
21. Bondeson, D.P. *et al.* Lessons in PROTAC Design from Selective Degradation with a Promiscuous Warhead. *Cell Chem Biol* **25**, 78-87.e75 (2018).
22. O'Hare, T., Eide, C.A. & Deininger, M.W. Bcr-Abl kinase domain mutations, drug resistance, and the road to a cure for chronic myeloid leukemia. *Blood* **110**, 2242-2249 (2007).

23. Eadie, L.N. *et al.* Asciminib Is Effective Against ABL1 Gene Fusions in Acute Lymphoblastic Leukemia but Only When the ABL1 SH3 Domain Is Present. *Blood* **142**, 1602 (2023).
24. McWhirter, J.R., Galasso, D.L. & Wang, J.Y. A coiled-coil oligomerization domain of Bcr is essential for the transforming function of Bcr-Abl oncoproteins. *Mol Cell Biol* **13**, 7587-7595 (1993).
25. Pendergast, A.M. *et al.* BCR-ABL-induced oncogenesis is mediated by direct interaction with the SH2 domain of the GRB-2 adaptor protein. *Cell* **75**, 175-185 (1993).
26. Simpson, G.L. *et al.* Identification and optimization of novel small c-Abl kinase activators using fragment and HTS methodologies. *Journal of medicinal chemistry* **62**, 2154-2171 (2019).
27. Yang, J. *et al.* Discovery and Characterization of a Cell-Permeable, Small-Molecule c-Abl Kinase Activator that Binds to the Myristoyl Binding Site. *Chemistry & Biology* **18**, 177-186 (2011).
28. Payne, N.C., Kalyakina, A.S., Singh, K., Tye, M.A. & Mazitschek, R. Bright and stable luminescent probes for target engagement profiling in live cells. *Nature Chemical Biology* **17**, 1168-1177 (2021).
29. Li, X. *et al.* Proteolysis-targeting chimeras (PROTACs) in cancer therapy. *Molecular Cancer* **21**, 99 (2022).
30. Smith, K.M., Yacobi, R. & Van Etten, R.A. Autoinhibition of Bcr-Abl through its SH3 domain. *Molecular cell* **12**, 27-37 (2003).
31. Amarante-Mendes, G.P., Rana, A., Datoguia, T.S., Hamerschlak, N. & Brumatti, G. BCR-ABL1 tyrosine kinase complex signaling transduction: challenges to overcome resistance in chronic myeloid leukemia. *Pharmaceutics* **14**, 215 (2022).
32. Million, R.P., Aster, J., Gilliland, D.G. & Van Etten, R.A. The Tel-Abl (ETV6-Abl) tyrosine kinase, product of complex (9;12) translocations in human leukemia, induces distinct myeloproliferative disease in mice. *Blood* **99**, 4568-4577 (2002).
33. De Keersmaecker, K. *et al.* Kinase activation and transformation by NUP214-ABL1 is dependent on the context of the nuclear pore. *Mol Cell* **31**, 134-142 (2008).
34. Wylie, A.A. *et al.* The allosteric inhibitor ABL001 enables dual targeting of BCR–ABL1. *Nature* **543**, 733-737 (2017).
35. Schoepfer, J. *et al.* Discovery of Asciminib (ABL001), an Allosteric Inhibitor of the Tyrosine Kinase Activity of BCR-ABL1. *Journal of Medicinal Chemistry* **61**, 8120-8135 (2018).
36. Yu, C. *et al.* High-throughput identification of genotype-specific cancer vulnerabilities in mixtures of barcoded tumor cell lines. *Nature Biotechnology* **34**, 419-423 (2016).
37. Tsherniak, A. *et al.* Defining a Cancer Dependency Map. *Cell* **170**, 564-576.e516 (2017).
38. Vasan, N., Baselga, J. & Hyman, D.M. A view on drug resistance in cancer. *Nature* **575**, 299-309 (2019).
39. Vinyard, M.E. *et al.* CRISPR-suppressor scanning reveals a nonenzymatic role of LSD1 in AML. *Nat Chem Biol* **15**, 529-539 (2019).
40. Freedy, A.M. & Liau, B.B. Discovering new biology with drug-resistance alleles. *Nature chemical biology* **17**, 1219-1229 (2021).
41. Hantschel, O. *et al.* A myristoyl/phosphotyrosine switch regulates c-Abl. *Cell* **112**, 845-857 (2003).
42. Cohen, P. The role of protein phosphorylation in human health and disease. The Sir Hans Krebs Medal Lecture. *European journal of biochemistry* **268**, 5001-5010 (2001).
43. Bartlett, G.J., Porter, C.T., Borkakoti, N. & Thornton, J.M. Analysis of catalytic residues in enzyme active sites. *J Mol Biol* **324**, 105-121 (2002).
44. Zhang, L., Riley-Gillis, B., Vijay, P. & Shen, Y. Acquired Resistance to BET-PROTACs (Proteolysis-Targeting Chimeras) Caused by Genomic Alterations in Core Components of E3 Ligase Complexes. *Mol Cancer Ther* **18**, 1302-1311 (2019).
45. Connor Payne, N. & Mazitschek, R. Tiny Titans: Nanobodies as Powerful Tools for TR-FRET Assay Development. *Analysis & Sensing* **2**, e202200020 (2022).
46. Frankenfield, A.M., Ni, J., Ahmed, M. & Hao, L. Protein Contaminants Matter: Building Universal Protein Contaminant Libraries for DDA and DIA Proteomics. *Journal of Proteome Research* **21**, 2104-2113 (2022).
47. Tyanova, S. *et al.* The Perseus computational platform for comprehensive analysis of (prote)omics data. *Nature Methods* **13**, 731-740 (2016).

48. Berman, H.M. *et al.* The Protein Data Bank. *Nucleic Acids Res* **28**, 235-242 (2000).
49. Abramson, J. *et al.* Accurate structure prediction of biomolecular interactions with AlphaFold 3. *Nature* **630**, 493-500 (2024).
50. Tokarski, J.S. *et al.* The structure of Dasatinib (BMS-354825) bound to activated ABL kinase domain elucidates its inhibitory activity against imatinib-resistant ABL mutants. *Cancer Res* **66**, 5790-5797 (2006).
51. Brown, N.R. *et al.* Effects of phosphorylation of threonine 160 on cyclin-dependent kinase 2 structure and activity. *J Biol Chem* **274**, 8746-8756 (1999).
52. Huang, J. & MacKerell, A.D., Jr. CHARMM36 all-atom additive protein force field: validation based on comparison to NMR data. *J Comput Chem* **34**, 2135-2145 (2013).
53. Lee, J. *et al.* CHARMM-GUI Input Generator for NAMD, GROMACS, AMBER, OpenMM, and CHARMM/OpenMM Simulations Using the CHARMM36 Additive Force Field. *J Chem Theory Comput* **12**, 405-413 (2016).
54. Eastman, P. *et al.* OpenMM 8: Molecular Dynamics Simulation with Machine Learning Potentials. *J Phys Chem B* **128**, 109-116 (2024).
55. Dolinsky, T.J., Nielsen, J.E., McCammon, J.A. & Baker, N.A. PDB2PQR: an automated pipeline for the setup of Poisson-Boltzmann electrostatics calculations. *Nucleic Acids Res* **32**, W665-667 (2004).
56. Dolinsky, T.J. *et al.* PDB2PQR: expanding and upgrading automated preparation of biomolecular structures for molecular simulations. *Nucleic Acids Res* **35**, W522-525 (2007).
57. Unni, S. *et al.* Web servers and services for electrostatics calculations with APBS and PDB2PQR. *J Comput Chem* **32**, 1488-1491 (2011).
58. Jurrus, E. *et al.* Improvements to the APBS biomolecular solvation software suite. *Protein Sci* **27**, 112-128 (2018).
59. Jo, S., Kim, T., Iyer, V.G. & Im, W. CHARMM-GUI: a web-based graphical user interface for CHARMM. *J Comput Chem* **29**, 1859-1865 (2008).
60. Jorgensen, W.L., Chandrasekhar, J., Madura, J.D., Impey, R.W. & Klein, M.L. Comparison of simple potential functions for simulating liquid water. *The Journal of Chemical Physics* **79**, 926-935 (1983).
61. MacKerell, A.D. *et al.* All-atom empirical potential for molecular modeling and dynamics studies of proteins. *J Phys Chem B* **102**, 3586-3616 (1998).
62. Ryckaert, J.-P., Ciccotti, G. & Berendsen, H.J.C. Numerical integration of the cartesian equations of motion of a system with constraints: molecular dynamics of n-alkanes. *Journal of Computational Physics* **23**, 327-341 (1977).
63. Ciccotti, G. & Ryckaert, J.P. Molecular dynamics simulation of rigid molecules. *Computer Physics Reports* **4**, 346-392 (1986).
64. Darden, T., York, D. & Pedersen, L. Particle mesh Ewald: An N·log(N) method for Ewald sums in large systems. *The Journal of Chemical Physics* **98**, 10089-10092 (1993).
65. Michaud-Agrawal, N., Denning, E.J., Woolf, T.B. & Beckstein, O. MDAnalysis: a toolkit for the analysis of molecular dynamics simulations. *J Comput Chem* **32**, 2319-2327 (2011).
66. Gowers, R.J. *et al.* MDAnalysis: A Python Package for the Rapid Analysis of Molecular Dynamics Simulations. *Proceedings of the 15th Python in Science Conference*, 98 – 105 (2016).
67. Corsello, S.M. *et al.* Discovering the anti-cancer potential of non-oncology drugs by systematic viability profiling. *Nat Cancer* **1**, 235-248 (2020).
68. Clement, K. *et al.* CRISPResso2 provides accurate and rapid genome editing sequence analysis. *Nature Biotechnology* **37**, 224-226 (2019).

Methods:

Chemical reagents and synthesis. Imatinib and asciminib were purchased from commercial sources and used without further purification (MedChemExpress, #HY-15463 and #HY-104010). Compounds were used as solutions in 100% DMSO and stored in the freezer at -20°C. Detailed descriptions for the synthesis of all chemical compounds and their characterization are provided in the Supplementary Methods.

Cell Culture. The following cell lines were used: K562 (ATCC, #CCL-243), KCL22 (ATCC, #CCL-3349), BV-173 (DSMZ, #ACC 20), EM-2 (DSMZ, #ACC 135), KYO-1 (DSMZ, #ACC 601), and stable Ba/F3 cells containing a TEL-ABL fusion, an E255V mutation, or a T315I mutation (gifts from J. Griffin and E. Weisberg). Cells were cultured in RPMI media (Gibco, #22400-089) with 10% fetal bovine serum (FBS; Gibco, #16140-071) and 1% penicillin-streptomycin (penstrep; Gibco, #15140-122). HEK293T cells (ATCC, #CRL-3216) were cultured in DMEM + GlutaMAX-I (Gibco, #10564-011) with 10% fetal bovine serum (FBS; Gibco, #16140-071) and 1% penicillin-streptomycin (penstrep; Gibco, #15140-122). Cell cultures were routinely checked for contamination with mycoplasma.

Cell viability assays. Compound stock solutions were prepared at a concentration of 10 mM in anhydrous DMSO and dispensed into white-bottom 384-well plates using a Tecan D300e digital dispenser. The compounds were plated either at a maximum concentration of 20 μM, followed by a 12-point, three-fold serial dilution, or at a maximum concentration of 10 μM, followed by a 14-point, two-fold serial dilution. All wells were normalized to a final DMSO concentration of 0.5% (v/v). Cells were seeded at a density of 2,000 cells per well in 25 μL of complete medium (containing 10% (v/v) FBS and 1% (v/v) penicillin/streptomycin) and incubated for 72 hours in a humidified incubator at 37°C with 5% CO_2. Cell viability was assessed using the CellTiter-Glo (Promega, G7572) assay, with reagent added at a volume equal to half the total well volume. Luminescence was measured using an Envision plate reader, and percentage viability was calculated relative to DMSO-only controls. Dose-response data were fitted to a four-parameter logistic curve using GraphPad Prism 10. EC_{50} values were determined from at least three independent replicates for all cell lines.

Protein expression and purification. *ABL* gene containing the SH3SH2 domain was cloned into the pET23a-His10X vector and expressed with a His tag. Plasmids were co-transfected with YpoH shuttle vector and transformed into BL21(DE3) competent cells (Thermo Fischer Scientific, #EC0114). The primary culture was inoculated using a single colony grown overnight in 10 ml of TB media containing 50µg/ml of ampicillin (GoldBio, #A-301-5) and spectinomycin (Millipore, #Y000065) at 37°C with shaking at 200 rpm. The secondary culture was prepared by inoculating 1% of the primary culture into 1 L of TB media with ampicillin and spectinomycin until it reached an OD_{600nm} of 0.3. The culture was moved to 18°C and further grown to OD_{600nm} of 0.6 before adding 0.5 mM isopropyl-β-D-1-thiogalactosidease (Thermo Fischer Scientific, #15529019) to induce protein expression. The culture was grown for 16 hours at 200 rpm and harvested by centrifuging at 6000 rpm (Thermo Fischer Scientific, Sorvall LYNX 6000) for 10 minutes at 4°C. The supernatant was discarded, and the cell pellet was resuspended in lysis buffer (20 mM Tris-Cl, pH 7.4, 150 mM NaCl, 1 mM TCEP, and 10% glycerol). All subsequent steps were performed at 4°C in the cold room. Cell lysis was initiated by adding 1 mg/ml of lysozyme, 0.5 mM PMSF (Thermo Fischer Scientific, #36987), and 1X protease inhibitor cocktail (Pierce, #A37989) (one tablet in 1 ml of lysis buffer). The cells were incubated for 1 hour with gentle rocking, and 0.5% Triton X-100 (Sigma, #X100) was added. The mixture was further incubated for 15 minutes, and the cells were sonicated using a 250-watt ultrasonic processor (Fischer Scientific, #SFX250) with a 6 mm diameter probe, applying a cycle of 8 seconds “ON” and 15 seconds “OFF” for 30 minutes. The lysate was centrifuged at 16000 rpm for 1 hour. The cell debris was discarded, and the protein was purified from the clarified lysate by affinity chromatography, incubating it with 1.4 ml of pre-equilibrated His-Pur Nickel nitriloacetic acid (Ni-NTA) resin (Thermo Scientific, #88221) overnight. The resin was washed thrice with 15 column volumes of washing buffer (20 mM Tris-Cl, pH 7.4, 500 mM NaCl, 40 mM imidazole, and 10% glycerol). Histidine-tagged protein was eluted using elution buffer (20 mM Tris-Cl, pH 7.4, 150 mM NaCl, 300 mM imidazole, and 10% glycerol). The collected protein was concentrated using 10 KDa cut-off Amicon spin concentrators (Millipore, #UFC901008), centrifuged at 3500 rpm for 45 min, and subjected to gel filtration chromatography using an AKTA pure system (Cytiva) and a HiLoad Superdex-200 column, 120 ml PG (Cytiva, #28989335) at a flow rate of 1 ml/min with running buffer (20 mM Tris-Cl, pH 7.4, 150 mM NaCl, 10% glycerol). The protein-containing fractions were analyzed using NuPAGE Bis-Tris gels with a 4-12% gradient (Thermo Scientific, #NP0321BOX). The purified protein was

quantified using BCA (Pierce, #A55864), snap-frozen in liquid nitrogen, and stored in aliquots at -80°C until future use.

Differential scanning fluorimetry. Thermal shift assays were performed using differential scanning fluorimetry (DSF) to assess the ABL thermal stability in the presence or absence of PHICS (**11**) or control ABL binder (**10**). Reactions were prepared in a final volume of 25 µl in DSF assay buffer (20 mM Tris-Cl-7.5, 150 mM NaCl and 1mM TCEP), containing 4 µM of purified ABL1-kinase domain, 10 µM of test compound or vehicle control, and Protein Thermal Shift™ dye (Thermo Scientific, #4461146) at a final dilution of 1:1000 from the manufacturer's stock. Samples were dispensed into a 384-well optical PCR plate (Applied Biosystems), sealed with optically clear film, and briefly centrifuged to remove bubbles. Thermal denaturation was monitored on a QuantStudio 7 Real-Time PCR System (Applied Biosystems) by increasing the temperature from 25 °C to 95 °C in 0.5 °C increments every 30 seconds. The melting temperature (Tm) was determined using the Protein Thermal Shift™ Software V1.4.

TR-FRET binding assay. TR-FRET assay was performed using CoraFluors, following previously reported procedures.[28, 45] In brief, anti-GST nanobody (Proteintech, #st-250) was buffer exchanged into reaction buffer (100 mM sodium carbonate buffer, pH 8.5 + 0.05% Tween20 [vol/vol]) using a 7 kDa cutoff centrifugal concentrator (Thermo Scientific, #89877) following the manufacturer's instructions. A 2.5 mM solution of CoraFluor-1-Pfp in dimethylformamide was added at 12–15 fold molar excess to the antibody and left to react for 1 hour at room temperature. Excess reagents and organic solvent were removed, and the buffer was changed to TR-FRET assay buffer (25 mM HEPES pH 7.4, 150 mM NaCl, 1 mM DTT, 0.5 mg ml^{-1} BSA, 0.005% TWEEN-20 [vol/vol]) using a 7 kDa cutoff centrifugal concentrator (Thermo Scientific, #89877).

Compounds were prepared in a 15-point, 2-fold serial dilution in a white 384-well plate (product reference) using a Tecan D300 digital dispenser. Compounds **10** and **11** were tested at a maximum concentration of 10 µM, and asciminib was tested at a maximum concentration of 1 µM. Next, TR-FRET assay buffer containing GST-ABL1 (Sino Biological, #11199-H09B, 2 nM), anti-GST nanobody conjugated to CoraFluor-1 (4 nM), and FITC-tracer (VS1231, 670 nM) were added, and the plate was incubated for 2 hours at room temperature. TR-FRET was measured on a Tecan Spark plate reader (SPARKCONTROL software version V2.1, Tecan Group) using an

excitation wavelength of 340/50 nm and reading emission at 490/10 nm and 520/10 nm. The delay time between excitation and measuring emission was set to 100 μs, and the signal was measured over 400 μs (integration time). Prism 10 was used to fit the data to a four-parameter dose–response curve. The binding affinities (K_D values) were calculated using the Cheng Prusoff equation (1):

$$K_{\mathrm{D}} = \frac{\mathrm{EC}_{50}}{1+\frac{[\mathrm{S}]}{K_{\mathrm{m}}}} \tag{1}$$

Where K_m is the affinity constant of the tracer, EC_{50} is the concentration at which the test ligand displaces 50% of the tracer, and [S] is the tracer concentration.

Analytical ultracentrifugation. Analytical ultracentrifugation (AUC) experiments were performed using a Beckman Optima XL-I analytical ultracentrifuge equipped with an absorbance-based detection system. A two-sector charcoal centerpiece with a 1.2 cm path length and sapphire windows was used. Purified proteins were dialyzed overnight against buffer A (25 mM Tris, pH 7.4, 150 mM NaCl) and samples were prepared by mixing ABL with compound **10**, **11**, or vehicle at an equimolar concentration of 1.5 μM while maintaining a DMSO concentration at 2%. The sample cell was loaded with 390 μL of protein solution, while the reference cell contained 400 μL of buffer A. Centrifugation was performed at 40,000 rpm (160,992 × g) at 20°C for 12–14 hours. Radial absorbance scans at 280 nm were collected every 3 minutes throughout the experiment and the resulting data analyzed with 'SedFit analysis' program using a continuous distribution(s) model based on the Lamm equation (2):

$$\frac{\partial \chi}{\partial t} = \frac{1}{r}\left\{\frac{\partial}{\partial r}\left[rD\frac{\partial \chi}{\partial r} - s\omega^2 r^2 \chi\right]\right\} \tag{2}$$

Where χ is the concentration, D is the diffusion coefficient and s is the sedimentation coefficient of the particle, t is the time, r is the radius from the center of rotation, and ω is the angular velocity of the rotor. Parameters including buffer density (ρ = 1.0059), buffer viscosity (η = 0.0105443 poise), and partial specific volume (υ = 0.73125) of protein were measured by the Sednterp program. Standard sedimentation coefficients of samples were represented as S20,w referring to sedimentation at 20°C.

NanoBiT ternary complex formation. Full-length *BCR-ABL1* (GenScript) was fused N-terminally with *LgBt* and *SmBt* (sequences shown in **Supplementary Table 1**) and cloned into the pCDNA3.1 vector backbone using NEBuilder HiFi DNA Assembly Master Mix (New England Bio Labs, #E2621L) according to the manufacturer's protocol. The NanoBiT assays were performed according to the manufacturer's protocol (Promega, #N2014) for adherent cells. Briefly, HEK-293T cells were grown overnight in DMEM (Thermo Fischer, #11965118) containing 10% FBS (Gibco, #16140071), washed twice with 1X PBS, trypsinized (Gibco, #25200056), and centrifuged for 5 minutes at 200 g. Cells were resuspended in growth media and counted on a CountessTM3 (Invitrogen, #AMQAZ2000). A transfection mixture was prepared by mixing BCR-ABL fusion constructs (1:3 ratio) with carrier DNA (Promega, #N2641), resulting in a DNA concentration of 10 µg/ml in 1 ml of Opti-MEM I without phenol red (Life Technologies, #11058-021) containing 1 % FBS. 35 µl of FuGENE HD Transfection Reagent (Promega, #E2311) was added to 1 ml of DNA mixture, the solution was mixed by inversion 5–10 times, incubated at room temperature for 30 minutes, and added to 20 ml of HEK-293T cell suspension of 0.2 million cells/ml in Opti-MEM assay solution. The resulting solution was gently mixed by inversion five times, and 95 µl of the final solution was dispensed in each well of the 96-well plate (20,000 cells/well, Corning, #3917). After 22–24 h, compounds or vehicle (DMSO) were added in 10 µl growth media, and 96-well plates were incubated at 37°C in a 5% CO_2-humidified atmosphere for 2 h. Compounds were tested in three independent replicates. After incubation, the plates were equilibrated at room temp for 15 minutes. The detection reagent was prepared by mixing 1 volume of Nano-GloR Live Cell Substrate (Promega, #N2011) with 19 volumes of Nano-GloR LCS Dilution Buffer. 50 µl was added to each well and the plate incubated for 2-3 minutes at room temperature before measuring the luminescence with 500 ms integration time was measured on an EnVision multimode plate reader (PerkinElmer). Raw data is processed by subtracting the background values and plotted using GraphPad Prism version 10.1.2.

Phosphoproteomic analysis. 50 x 10^6 K562 cells were treated for 4 hours with DMSO, **11** (1 µM), **10** (2 µM), or asciminib (1 µM) at a density of 1x10^6 cells per ml. After compound treatment, cells were washed with ice-cold PBS, pelleted, and stored at -80 ˚C until further use. The cell pellet was then treated (with gentle end-over-end-rotation) for one hour with M-PER (Mammalian Protein Extraction Reagent, ThermoFisher, #78501) supplemented with 1X cOmplete EDTA-free Protease Inhibitor (Roche, #4693159001) and 1X PhosSTOP Phosphatase Inhibitor (Roche, #4906837001). The cell lysates were centrifuged at 16,000 x g for 10 minutes at

4°C, and the total protein concentration in the resulting supernatant was estimated with a Pierce BCA Protein Assay Kit (ThermoFisher, #23225). Immunoprecipitation (IP) of the BCR-ABL protein was performed using the Dynabeads Protein G (ThermoFisher, #10004D) according to manufacturer instructions, using an ABL primary antibody (Cell Signaling Technology, #2862) at a 1:100 dilution (1 µg ABL Ab / 100 µg total lysate) and overnight protein binding at 4 °C on a rotator. Unbound and non-specific proteins were washed out, and bead-bound proteins were eluted with 1X Sample buffer (BioRad, #1610747) using 2-mercaptoethanol and heating at 95°C for 5 minutes. IP eluates were resolved by SDS-PAGE, gel bands excised, and proteins reduced with 1 mM dithiothreitol (DTT) at 60°C for 30 minutes. Samples were alkylated with 5 mM iodoacetamide for 15 minutes at room temperature in the dark and subjected to in-gel trypsin digestion. Briefly, gel pieces were washed, dehydrated with acetonitrile, and dried in a speed-vac (Eppendorf Vacufuge Plus) before rehydration at 4°C with 50 mM ammonium bicarbonate containing 12.5 ng/µL sequencing-grade trypsin (Promega, #V5111). Samples were digested overnight at 37°C. Peptides were then extracted with 50% acetonitrile and 1% formic acid, dried in a speed-vac (Eppendorf Vacufuge Plus), and stored at 4°C until analysis. Phosphoproteomic analysis was performed at the Taplin Biological Mass Spectrometry Facility (Harvard Medical School). In brief, samples were reconstituted in 5–10 µl of HPLC solvent A (2.5% acetonitrile, 0.1% formic acid) and separated using a nano-scale reverse-phase HPLC capillary column (100 µm inner diameter x ~30 cm length) packed with 2.6 µm C18 silica beads. Peptides were loaded via a Thermo EASY-LC system (Thermo Scientific) and eluted using a 130 min gradient (0.0-1.0 min: 3%-5% ACN, 1.0-69.0 min: 5%-25% ACN, 69.0-89.0 min: 25%-40% ACN, 89.0-104.0 min: 40%-60% ACN, 104-120 min: 95% ACN) at a flow rate of 0.3 µL/min. Eluted peptides were subjected to electrospray ionization and analyzed on an Orbitrap Fusion Lumos mass spectrometer (Thermo Scientific). The raw data were analyzed using Proteome Discoverer 2.5 software package (Thermo Scientific). Sequest HT was used to search against human tyrosine-protein kinase Abl (P00519) with a precursor mass tolerance of 10 ppm and fragment mass tolerance of 0.6 Da. A maximum of two missed cleavages and a minimum peptide length of six were selected. Search parameters included dynamic modifications for methionine oxidation (15.995 Da), tyrosine phosphorylation (79.966 Da), N-terminal glutamate cyclization, and acetylation, as well as static cysteine alkylation (+57.021 Da). Target Decoy PSM Validator was applied with a false discovery rate (FDR) of 1%. IMP-ptmRS was used to calculate phosphorylation site probabilities, and phosphopeptide-containing groups were

filtered. Labeled and unlabeled peptide precursor ion intensities were used to estimate labeling efficiency. The results were exported and analyzed using GraphPad Prism 9.0.

Global phosphoproteomic analysis. K562 cells were adjusted to a density of 1×10^6 cells/mL in complete growth media and treated in quadruplicate with vehicle (DMSO), 2 μM control compound (**10**), or 1 μM PHICS (**11**) for 4 hours. Upon completing the treatment, cells were harvested and washed with ice-cold PBS. For phosphoproteomics, 23×10^6 cells were pelleted and lysed in EasyPep Lysis Buffer (Thermo #A45735) with protease and phosphatase inhibitors (Thermo #78444), following the manufacturer's protocol. Protein concentration was determined using the Rapid Gold BCA Kit (Thermo #A53225) and ~500 μg of lysate were reduced with 5 mM TCEP (Thermo #20490) at 60°C for 30 min, alkylated with 10 mM iodoacetamide (Thermo #122270250) before quenching excess reagent with 10 mM DTT (Thermo #20290), and purified using SP3 resin beads (Hydrophilic and Hydrophobic, Thermo #09-981-121; 09-981-123). Next, Trypsin/Lys-C Mix (Promega #V5072) in 200 mM EPPS (pH 8.5) was added at a 1:100 ratio to digest the protein lysate at 37°C for ~16 hours. Resulting peptides were in 30% acetonitrile and labeled with TMTpro 18-plex reagents (Thermo #A52045) at a 1:1 ratio. Upon confirming the labeling efficiency (>95%), the reactions were quenched with 50% hydroxylamine (Thermo #90115). For total proteomic analysis, ~100 μg of pooled sample was cleaned using the SP3 resin protocol described above and fractionated with the Pierce High pH Reversed-phase Peptide Fractionation Kit (Thermo #84868). The resulting 10 fractions were subsequently analyzed by LC-MS/MS on an Orbitrap Eclipse Tribrid instrument as described below. For phosphoproteomic analysis, the remaining samples were dried by vacuum centrifugation, desalted (Peptide Desalting Spin Columns, Thermo #89851), and enriched for phosphotyrosine peptides using 30 μL of P-Tyr-1000 (Cell Signaling #8954) conjugated to protein A agarose (MilliporeSigma #11134515001) in IAP buffer (6-hour incubation at 4°C). After washing, phosphopeptides were eluted in 100 mM formic acid, desalted, and analyzed by LC-MS/MS.

For LC-MS/MS analysis, samples were reconstituted in 2% acetonitrile containing 0.2% formic acid, sonicated, and centrifuged at 10,000g for 1 min. Supernatants were transferred to LC-MS vials (Thermo Fisher, #6PK1655) and loaded onto a Vanquish Neo UHPLC system (Thermo Fisher) coupled to an Orbitrap Eclipse mass spectrometer with a NanoFlex ion source. For total proteomics analysis, samples were separated on a 60 cm column (IonOpticks, #AUR3-60075C18-TS) using a 120-minute gradient (0.0–1.0 min, 3%–5% ACN, 1.0–69.0

min, 5%–25% ACN, 69.0–89.0 min 25%–40% ACN, 89.0–104.0 min 40%–60% ACN, 104–120 min 95% ACN, wash) at a flow rate of 0.3 µL/min. MS1 data were acquired in Orbitrap mode with a resolution of 120,000, AGC target 400000, and maximum injection time 50 ms. Charge states from 2+ to 6+ were included, and a dynamic exclusion time of 60 seconds was used. MS2 scans were isolated with quadruple and fragmented using HCD with a fixed collision energy of 35% and a 0.7 m/z isolation window. The normalized AGC target for MS2 was set to 200%, and fragment ions were detected in the Orbitrap at a resolution of 50,000 with a defined first mass of m/z 120. Phosphoproteomic samples were separated on the 60 cm IonOpticks column (#AUR3-60075C18-TS) using a 180-minute gradient (0.0–6.0 min, 3%–5% ACN, 6.0–121.0 min, 5%–25% ACN, 121.0–152.0 min 25%–40% ACN, 152.0–161.0 min 40%–60% ACN, 161–180 min 95% ACN, wash) at a flow rate of 0.3 µL/min and the same MS acquisition parameters as described above for the total proteomic analysis.

Proteome Discoverer 2.5 (Thermo Fisher) was used to process the raw data, using Sequest HT for peptide identification against the human reference proteome (Uniprot proteome ID: UP000005640_9606) and a contaminant database.[46] The search criteria allowed up to two missed cleavages and included peptides with at least 6 amino acids. Precursor mass tolerance was set at 10 ppm, and fragment mass tolerance was fixed at 0.02 Da. Dynamic modifications included methionine oxidation (+15.995 Da) and phosphorylation (+79.966 Da) on serine, threonine, and tyrosine. N-terminal dynamic protein modifications included acetylation (+42.011 Da), methionine loss (-131.040 Da), and methionine loss together with acetylation (-89.030 Da). Static modifications included cysteine alkylation (+57.021 Da) and conjugation with TMT reagent (+304.207 Da) on peptide N-termini and lysines. Peptide-spectrum match (PSM) was validated using Percolator and a false discovery rate (FDR) of 0.01. IMP-ptmRS node was used for phosphosite localization. TMTpro isotopic impurity corrections were applied and the resulting data was exported as CSV for importing into Perseus,[47] in which reporter ion abundances were $\log_2$-transformed and normalized by subtracting each column's median, replicates were grouped according to experimental conditions, and Welch's t-tests were performed to identify phosphopeptides with significantly altered abundances (see **Supplementary Data 1**). Volcano plots were prepared in GraphPad Prism.

Molecular Dynamics (MD) simulations. Since no crystal structures of activated (i.e., DFG-in) BCR-ABL in complex with ATP · Mg^{2+} are currently available in the Protein Data Bank,[48] structural models were generated via AlphaFold3.[49] The two top-ranked predictions were selected for MD simulations. In addition, a "hand-built"

model was also constructed by aligning the alpha carbons of 2GQG[50] and 1B38[51], taking the coordinates of BCR-ABL from 2GQG and the coordinates of ATP · Mg^{2+} from 1B38. For each model, four independent MD simulations were performed for four different states; i.e., apo wild-type (WT), apo Y253TP2, holo WT, and holo Y253TP2—using the CHARMM36 force field[52] in OpenMM 8.2.[53, 54] Apoenzymatic states were created by removing the ATP · Mg^{2+} ligand from the holoenzymatic structures. In the simulations, the protonation states of titratable residues were assigned using the PDB2PQR software package,[55-58] and the CHARMM-GUI web server[59] was used to solvate and minimize the resulting structures in 150 mM NaCl solutions of TIP3P water.[60, 61] The box length of the simulation cell is in the range of 83–85 Å. Every system was equilibrated for 100–200 ns at 303.15 K and 1 bar with a 2 fs timestep, followed by 300 ns of production MD. All bonds involving hydrogen atoms were constrained with the SHAKE algorithm.[62, 63] Nonbonded interactions were treated with a van der Waals (vdW) force-switching function employing a switching distance of 10 Å and cutoff distance of 12 Å. Electrostatic interactions were calculated using the Particle-Mesh-Ewald approach, with a real space cutoff of 12 Å and an error tolerance of 5×10^{-4}.[64] Temperature was regulated by a Langevin thermostat with a collision frequency of 1 ps^{-1}, and pressure was maintained by a Monte Carlo barostat with a coupling frequency of 5 ps^{-1}. Analysis of the resulting trajectories was achieved utilizing the MDAnalysis program.[65, 66] Representative snapshots were obtained by *k*-means clustering of each system's two largest principal components. Electrostatic potential calculations of the WT and Y253TP2 apoenzymes were performed using the Adaptive Poisson–Boltzmann Solver[57, 58] plugin for PyMOL (Schrödinger INC., Version 3.0) at a temperature of 303.15 K and salt concentration of 150 mM; partial charges were taken from the CHARMM36 force field,[52] and vdW radii were used to define atomic volumes. All three structural models exhibited consistent qualitative behavior. That is, phosphorylation of Y253 substantially alters the P-loop's conformation and leads to the formation of a stable ionic cluster between ATP's triphosphate moiety, Y253TP2's phosphate group, R367, and several sodium ions. Results from simulations starting from the top-ranked AlphaFold3-generated model were used for all figures.

Immunoblotting. K562 cells were counted, and 3.5×10^6 cells (at 1×10^7 cells per ml) were taken for each condition. DMSO and solutions of the tested compounds (**10**, 2 μM; **11**, 1 μM) were prepared in complete media with a final concentration of 0.1% DMSO and were added to the cells. The cells were then incubated for different times depending on the effect to be measured: 4 hours for detecting BCR-ABL autophosphorylation (pY70,

pY226, and pY393), 7 hours for downstream signaling (pERK, pSTAT5), and 70 hours for pCRKL signaling and Caspase8 and PARP cleavage. After incubation, the cells were harvested, washed with ice cold 1× PBS, and stored at -80°C until further processing. The cells were lysed using M-PER lysis buffer (ThermoScientific, #78505) containing cocktails of protease (Roche, #4693159001) and phosphatase inhibitors (Roche, #4906837001). The total lysates were spun at 16,000 g for 10 min at 4°C, and the total protein concentration in the supernatant was estimated by BCA (cat# 23225, Thermo Scientific). An equal amount of total lysate (1 µg/µl) was run on the automated simple western (Jess) using all required reagents from ProteinSimple. The results were analyzed using the Compass SW software. Primary antibodies used for detecting the autophosphorylation of BCR-ABL, including pY393 (Cell Signaling, #2865), pY226 (Cell Signaling, #2861), pY70 (Cell Signaling, #3098), and cABL (Santa Cruz Biotechnology, #SC-23), as well as antibodies for detecting downstream signaling, such as pSTAT5 (Cell Signaling, #9351), STAT5 (Cell Signaling, #94205), pERK1/2 (Cell Signaling, #4370S), ERK1/2 (Cell Signaling, #4696S), pCRKL (Cell Signaling, #34940), CRKL (Cell Signaling, #38710), caspase-8 (Cell Signaling, #4790), PARP (Cell Signaling, #9532), and the β-actin (Cell Signaling, #4967, 3700) and GAPDH (Cell Signaling, #2118, 97166) loading controls. All primary antibodies were used at 1:50 dilutions. Secondary antibodies: anti-rabbit-HRP (cat# 042-206, Protein Simple), used without further dilution, and anti-mouse-NIR (cat# 043-821, Protein Simple), used at 1:20 dilution. BCR-ABL phosphosites were mapped to the human ABL1 sequence (UniProt accession: P00519). For antibodies that did not work in automated Simple Western, conventional Western blots were performed. Briefly, cell lysates containing equal amounts of total protein (20 µg) were heated with Laemmli reducing SDS sample buffer at 95–100°C for 5 min. The protein samples were then resolved using NuPAGE gels (4-12%), which were then dry-transferred to nitrocellulose membranes (iBlot2). The membranes were blocked with 5% milk in 1× TBST buffer, followed by incubation overnight at 4°C (in a cold room) on an orbital shaker with a 1:1000 dilution of primary antibodies. The membranes were then washed with 1× TBST buffer and were incubated further with the appropriate secondary antibodies, IRDye800CW-conjugated donkey anti-mouse (1:10,000; LiCor, #926-32212), and IRDye680RD-conjugated donkey anti-rabbit (1:10,000; LiCor, #926-68073), for 1 hour at room temperature. The membranes were again washed with 1× TBST buffer. Fluorescent blots were developed using the LiCor Odyssey CLx Imaging System. Uncropped western blot images are shown in **Supplementary Figs. 10–12**.

Gene expression analysis. K562 cells were treated with either DMSO (vehicle), asciminib (100 nM), PHICS (**11**; 1 μM), or control (**10**; 2 μM) for 6, 12, or 24 hours in biological quadruplicate. After the indicated treatment time, the cells were harvested, pelleted, and shipped on dry ice to Genewiz (South Plainfield, NJ) for RNA extraction and RNAseq analysis. Genewiz first isolated total RNA using the RNeasy RNA isolation kit (Qiagen, #74104), and the quality of the sample extraction was analyzed via Nanodrop and Agilent Tapestation. mRNA isolation/library prep was performed by Poly-T oligonucleotide-mediated mRNA extraction through hybridization of the mature mRNA Poly-A tail using NEBNext Ultra II Directional RNA Library Prep Kit for Illumina (New England Biolabs, #E7760S). The overall quality of the library was analyzed using an Agilent Tapestation. The enriched mRNA was reverse transcribed into DNA with subsequent second-strand synthesis. Sequencing was performed by Genewiz using Illumina HiSeq, 2× 150 bp configuration, single-index sequencing platform. Sequencing depth was performed at ~37 M reads per sample, generating ~15 GB of data per sample. The data was downloaded via FTP from Illumina as a fastq file for analysis. Sequencing alignment and data analysis were performed by the Harvard Medical School Joslin Diabetes Center Bioinformatics & Biostatistics core. The aligned sequencing data were further investigated using moderated t-tests, principal component analysis, gene set enrichment analysis (GSEA), expression heatmaps, gene ontology (GO), Reactome, TFT pathway analysis, and KEGG pathway analysis. Weighed p-values, FDR, log fold-change, and fold-change of each treatment compared to the vehicle (DMSO) condition are provided in **Supplementary Data 2**.

PRISM multiplexed cancer cell line screening. This assay was performed in collaboration with the Broad Institute PRISM team as described previously[36, 67]. Two PRISM cell line collections were used: PR500, which consists exclusively of adherent cell lines, and PR300+, which includes both suspension and adherent cell lines. Briefly, lentivirally barcoded cells were cultured in pools of 20–25 cell lines in 384-well plates, with each pool consisting of mixed lineages grouped by doubling rate. Cells were treated with either compound **11** (eight-point, three-fold serial dilution: 0.01 nM to 20 μM), compound **10**, Imatinib (eight-point, three-fold serial dilution: 0.005 nM to 10 μM), or with vehicle control, and incubated for 120 hours. Treatments were performed in three independent replicates. Following incubation, cells were lysed, and genomic DNA was extracted from the pooled cells. The unique DNA barcodes identifying each cell line were amplified by PCR and hybridized to Luminex beads conjugated with complementary antisense barcodes. The beads were then incubated with streptavidin-

phycoerythrin to fluorescently label biotin moieties, and fluorescence signals were detected using Luminex FlexMap machines. Data were processed using a previously established standardized R pipeline (https://github.com/broadinstitute/prism_data_processing) to estimate drug sensitivities across different concentrations and fit dose-response curves. The area under the dose-response curve (AUC) was used to quantify and compare drug sensitivity across cell lines. Cell line annotations were obtained from the DepMap platform (https://depmap.org/portal/) to correlate target fusion gene expression with drug sensitivity. Detailed annotations of all cell lines and their respective AUC-based responses to compounds **10** and **11** are provided in **Supplementary Data 3**.

sgRNA pooled cloning and CRISPR suppressor screening. CRISPR suppressor screens were performed in K562 cells, which harbor the *BCR-ABL1* fusion gene and are sensitive to ABL1 knockout, as annotated by the DepMap CRISPR and RNAi database (https://depmap.org/portal/). To generate in situ mutational diversity of BCR-ABL, SpCas9 and a pool of all possible sgRNAs with an NGG PAM site within the *ABL1* coding sequence were used. sgRNAs were filtered to include only those with an off-target score (MIT Specificity Score) greater than 20 to minimize off-target effects. A total of 78 sgRNAs targeting non-essential genes (negative controls) and three sgRNAs targeting essential genes (positive controls) were also included in the pool. A complete list of protospacers targeting *ABL1* and control genes is provided in **Supplementary Data 4**. The sgRNA library was synthesized as an oligonucleotide pool with corresponding homology arms for Gibson assembly (Twist Bioscience) and cloned into an Esp3I-digested lentiCRISPRv2 vector (Addgene #52961, a gift from Feng Zhang) using NEBuilder HiFi DNA Assembly Master Mix (New England Bio Labs, #E2621L) according to the manufacturer's protocol. The pooled plasmid library was electroporated into Endura DUO cells (Biosearch Technologies, #60242) using a Gene Pulser Xcell Electroporation System (Bio-Rad). To ensure adequate sgRNA coverage, the number of transformed cells was maintained at more than 1,000-fold the number of sgRNAs in the library. Lentiviral particles were produced using pMD2.G (Addgene #12259) and psPAX2 (Addgene #12260) packaging plasmids (both gifts from Didier Trono) and transduced into K562 cells via spinfection (1,800 rcf for 90 min) at a low multiplicity of infection (MOI < 0.3) to ensure integration of a single sgRNA per cell. Cells then underwent puromycin selection for >10 days and were split into three independent replicates for treatment with vehicle (0.1% DMSO), asciminib, or PHICS (**11**) over a total of 63 days (details for

the drug-dosing are provided in **Supplementary Table 2**). Cell growth was recorded every 3–5 days to ensure the selection of drug-resistant cells. At 7, 21, and 63 days post-treatment, cells were harvested for sgRNA enrichment analysis. Genomic DNA was extracted using a QIAamp DNA Blood Mini Kit (Qiagen, #51104) following the manufacturer's protocol. The sgRNA regions were PCR-amplified to incorporate Illumina adapters, and the coverage and distribution of the sgRNA library were assessed using MiSeq (Illumina). Data analysis was performed using previously described Python scripts.[39] Briefly, sgRNAs were mapped to the protein amino acid positions based on the predicted cut site coordinates within the *ABL1* (NP_005148.2) coding sequence. Sequencing reads uniquely matching each sgRNA were converted to reads per million, increased by a pseudocount of 1, log2-transformed, and averaged across replicates for each condition. The values were normalized to the plasmid library. sgRNA resistance scores were then calculated by normalizing to the mean score of the negative control sgRNAs within each condition and subtracting the score in the vehicle condition from that in the compound-treated condition at matching time points. Final values were z-scored based on the mean and standard deviation of the negative control distribution.

Validation of sgRNAs from the CRISPR-resistance screening. The six most enriched sgRNAs (sgD325, sgD504, sgK508, sgN670, sgS676, and sgL686) from the pooled CRISPR suppressor screen were cloned into the LentiCRISPRv2 plasmid for validation. The vector was digested with BsmBI (New England Biolabs, #R07399L) to generate 3' and 5' overhangs. Single-stranded protospacer oligonucleotides with complementary overhangs (Eton Bioscience) were phosphorylated using T4 Polynucleotide Kinase (New England Biolabs, #M0201S), annealed, and ligated into the digested vector with the Quick Ligation Kit (New England Biolabs, #M2200S). Oligonucleotide sequences for sgRNA validation are listed in **Supplementary Table 3**. Lentiviral particles were produced and transduced into K562 cells as described for library preparation. Transduced cells underwent a 63-day drug selection following the outline in **Supplementary Table 2**. Growth rates were measured every 3–5 days to ensure the selection of drug-resistant cells.

Genotyping and indel sequencing of drug-resistant variants. Genomic DNA from drug-selected cells was extracted using the QIAamp DNA Blood Mini Kit (Qiagen, #51104), following the same protocol used for sgRNA distribution analysis. At least 1 µg of genomic DNA was used as the template for the first round of PCR to amplify

gene-specific amplicons with common overhangs (20 cycles, NEBNext Ultra II Q5 Master Mix, New England Bio Labs, #M0544L). For cDNA analysis, total mRNA was isolated from drug-selected cells using the RNeasy Mini Kit (Qiagen, #74106). cDNA was synthesized by RT-PCR using the SuperScript III First-Strand Synthesis SuperMix (Invitrogen, #18080-400). The resulting cDNA was then amplified in a first round of PCR, following the same conditions as genomic DNA amplification. PCR products were diluted 1:10 and subjected to a second round of PCR using primers with barcoded Illumina adapters (10 cycles, NEBNext Ultra II Q5 Master Mix). Primer sequences for both PCR rounds are provided in **Supplementary Table 4**. The final PCR products were purified using SPRIselect bead clean-up (Beckman Coulter Life Sciences, #B23317), isolating fragments of approximately 500 bp according to the manufacturer's protocol. The concentration of purified amplicons was determined by qPCR using the KAPA Library Quantification Kit (Roche, #07960140001) and adjusted to 2 nM. Final amplicons were sequenced on an Illumina MiSeq using a Nano Kit v2 (Illumina, #MS-103-1003) according to the manufacturer's instructions. Sequencing reads were aligned to their reference amplicons using CRISPResso2 (ref[68]), and allele frequencies were calculated (see **Supplementary Data 5,6**).